An efficient algorithm for sampling the shear-modulus reduction curve in the context of wave propagation using the elastoplastic Iwan model

Simon Chabot, D. Mercerat, N Glinsky, Luis Fabian Bonilla

Geophysical Journal International

Geophys. J. Int. (2022) **228,** 1907–1917
Advance Access publication 2021 October 23
GJI Seismology

https://doi.org/10.1093/gji/ggab431

An efficient algorithm for sampling the shear-modulus reduction curve in the context of wave propagation using the elastoplastic Iwan model

S. Chabot,[1,2,*] E.D. Mercerat,[2] N. Glinsky[2] and L.F. Bonilla[1]

[1] *GERS Department, Université Gustave Eiffel,* 77447 *Marne la Vallée, France*
[2] *CEREMA Méditerranée, Project-Team Repsody,* 06903 *Sophia Antipolis, France. E-mail: diego.mercerat@cerema.fr*

Accepted 2021 October 21. Received 2021 October 13; in original form 2020 August 25

SUMMARY

The elastoplastic Iwan model has been used since the end of the 1970s to simulate nonlinear soil behaviour in seismic wave propagation. In this work, we present an automatic algorithm to efficiently sample the shear-modulus reduction curve in function of shear deformation, which constitutes the exclusive ingredient of the elastoplastic model. This model requires the data from the shear- modulus reduction as a function of shear deformation, which are readily available in the literature and from specific laboratory tests. The method involves a discretization and interpolation of these data to be used. The quality of the solution depends on the number of interpolated points. However, a larger number of them produce an increase of the computational time. To overcome this, we present an automatic algorithm to efficiently sample the shear-modulus reduction curve. We numerically prove that the chosen discretization of the curve has a strong impact on the calculation load, in addition to the well-known dependence on the input motion amplitude level. Two tests of nonlinear wave propagation in 1-D and 3-D media show the clear gain in computation time when using the proposed automatic sampling algorithm.

Key words: Computational seismology; Site effects; Wave propagation; Earthquake ground motions.

1 INTRODUCTION

Recent advances in computer architectures render large-scale seismic wave propagation simulations feasible in heterogeneous geological media. Several numerical methods are nowadays available and the final choice of the method is clearly problem dependent (Poursartip *et al.* 2020). In the context of earthquake engineering, the accurate simulation of strong ground motions near the free surface led to the development of different methods that take into account complex (nonlinear) soil rheologies. In general, elastic *P*- and *S*-wave velocities decrease drastically as they approach the free surface. In addition, the strength of the shallow crust may be small due to the low con- fining pressure. When the incident wavefield is strong enough, the material behaves nonlinearly, which results in a reduction of the wave speed during strong motion. This speed reduction makes that computational meshes of numerical models should drastically be refined in these regions when dealing with wave propagation in nonlinear media. Such conditions become a bottleneck for many large-scale numerical studies. The computation time of such simulations can become out of range and the frequent question that is asked is how much does a nonlinear simulation cost compared to the linear case. Therefore most numerical simulations including nonlinear rheologies are done in 1-D layered media (i.e. soil columns when restricted to the upper tens or hundreds of metres) and there are relatively few codes available for wave propagation in complex 2-D and 3-D nonlinear media.

In the recent study of Moczo *et al.* (2018), it has been stated the importance of taking into account 2-D/3-D effects for realistic estimations of earthquake ground motions. Some first attempts have emerged in the context of finite differences (Gélis & Bonilla 2012, 2014), finite elements (Taborda *et al.* 2012; Chen *et al.* 2015) and high-order (*spectral*) finite elements (Prisco *et al.* 2007; Oral *et al.* 2017, 2019). Among these approaches, one of the most used elastoplastic model in computational engineering seismology is the *Iwan* model [also known as Masing–Prandtl–Ishlinskii–Iwan (MPII) model] that allows to follow any shear-modulus reduction curve and also take into account hysteretic soil behaviour. The model has been extensively used in 1-D seismic wave modelling since the pioneering work of Joyner & Chen (1975). Its application for nonlinear wave propagation in higher spatial dimensions is becoming a reality (Chabot 2018; Oral *et al.* 2019). The Iwan model has been widely used in the recent years to take into account

*Now at: LogiLab, Paris, France

elastoplastic behaviour in geomaterials, but almost all the applications focus exclusively on 1-D wave propagation, and therefore with relatively low computational cost (i.e. soil columns of just one vertical column of calculation grid nodes). The model is based on a series of elements that must be defined at each node of the nonlinear domain. In realistic regional wave propagation simulations, with hundreds or millions of nodes within sedimentary layers with nonlinear behaviour, the computational cost of the simulation may become out of reach. The main objective of this work is to introduce an efficient technique to sample the shear-modulus reduction curve, which characterizes the nonlinear behaviour leading to a significant reduction in computational cost. The Iwan model can reproduce any type of decay curve (interpolated from laboratory data or from bibliography). The proposed technique can be used regardless of the numerical method chosen to solve the elastodynamic system of equations, which makes it interesting for all users of Iwan type models.

2 ELASTOPLASTIC IWAN MODEL

To solve the system of elastodynamic equations, an explicit relation between stress and strain is needed, this is the so-called material constitutive model. As a fully coupled numerical simulation is proposed (i.e. including the three components of motion), this model should take into account all stress-strain components, even if some of them are set to zero when the propagation is unidimensional (Gandomzadeh 2011; Santisi d'Avila *et al.* 2012; Chabot 2018). In the incremental theory of plasticity, the total strain increment is classically decomposed in its elastic and plastic contributions $\boldsymbol{\varepsilon} = \boldsymbol{\varepsilon}_E + \boldsymbol{\varepsilon}_P$. While the elastic part is completely defined by the linear Hooke's law ($\boldsymbol{\varepsilon}_E = \boldsymbol{C}^{-1}\boldsymbol{\sigma}$), the plastic strain needs to be determined by the yield criterion, the hardening law and a flow rule. The yield criterion is generally defined by a yield surface $F(\boldsymbol{\sigma}) = 0$ in the stress space, the hardening law defines how these surfaces change in size and shape when yielding occurs, and the flow rule describes how the plastic strains behave when yielding (Lubliner 1990). In this framework, we use the MPII model that has already been adopted in previous studies dealing with nonlinear wave propagation for site effect assessment. In addition, it naturally reproduces the hysteresis loops satisfying Masing criteria (Joyner & Chen 1975; Gandomzadeh 2011; Santisi d'Avila *et al.* 2012; Pham 2013; Mercerat & Glinsky 2015; Oral *et al.* 2017; Chabot *et al.* 2018). The MPII type elastoplastic models are based on a series of nested yield surfaces defined by simple *Iwan elements* each of them consisting of an elastic (linear) spring and a sliding (perfectly plastic) element. These elements arranged in a series-parallel configuration, are better suited to a formulation that separates elastic and plastic strain increments. We focus on the implementation of the method. For a detailed presentation of the model, we refer to the seminal articles of Iwan (1966, 1967), Joyner & Chen (1975) and Segalman & Starr (2008). The setting of model parameters (i.e. stiffness and yield stress for each element) requires only the shear-modulus reduction curve as function of shear strain, which can be readily obtained from laboratory tests or the literature for different soil classes (Vucetic, Mladen & Dobry, Ricardo 1991; Ishibashi & Zhang 1993; Darendeli 2001). One remarkable characteristic of the model is that it allows to follow any laboratory curve of shear-modulus decay. The only free parameter is the number of elastoplastic elements to be used to discretize the shear-modulus reduction curve. First attempts to evaluate the impact on the number of elements and the numerical method used to solve the elastodynamic equations can be found in Gandomzadeh (2011) and Mercerat *et al.* (2015). Finally, we note that the Iwan constitutive model is not strain rate dependent, and therefore all damping comes from hysteresis. As already proposed by Joyner & Chen (1975); Joyner *et al.* (1981), it is also possible to couple the hysteretic damping with a viscoelastic one by adding a dashpot element in parallel to take into account viscous damping at low strain ($<10^{-6}$).

2.1 Implementation of the MPII model

The MPII elastoplastic model is based on a series of nested fracture surfaces defined by the *Iwan units (or elements)*, each of them consisting of an elastic spring and a sliding element. These units can be arranged in a parallel-series or a series-parallel configuration (Iwan 1966, 1967). The second is better adapted to a formulation allowing to separate elastic and plastic strain increments, given a stress increment. The model parameters, the stiffness and the yield stress for each element, only require the shear-modulus reduction curve as a function of the shear strain. The following implementation, which is largely inspired by Joyner (1975), is assigned to each node belonging to a nonlinear medium of the computational domain.

For the remainder, the following vector notation is used for the strain and the stress tensors components :

$$\vec{\varepsilon} = \left(\varepsilon_{xx}, \varepsilon_{yy}, \varepsilon_{zz}, \varepsilon_{xy}, \varepsilon_{xz}, \varepsilon_{yz}\right) = \left(\varepsilon_1, \varepsilon_2, \varepsilon_3, \varepsilon_4, \varepsilon_5, \varepsilon_6\right), \tag{1}$$

$$\vec{\sigma} = \left(\sigma_{xx}, \sigma_{yy}, \sigma_{zz}, \sigma_{xy}, \sigma_{xz}, \sigma_{yz}\right) = \left(\sigma_1, \sigma_2, \sigma_3, \sigma_4, \sigma_5, \sigma_6\right). \tag{2}$$

The total strain increment $\mathrm{d}\vec{\varepsilon}$ is subdivided into its elastic $\mathrm{d}\vec{\varepsilon}_v$ and plastic part $\mathrm{d}\vec{\varepsilon}_p$ such that $\mathrm{d}\vec{\varepsilon} = \mathrm{d}\vec{\varepsilon}_v + \mathrm{d}\vec{\varepsilon}_p$. The relation between the increment of the mean stress $\sigma_M = (\sigma_1 + \sigma_2 + \sigma_3)/3$ and the volumetric deformation $\varepsilon_v = \varepsilon_1 + \varepsilon_2 + \varepsilon_3$ is linear and can be written as

$$\mathrm{d}\varepsilon_v = \mathrm{d}\sigma_M / K, \qquad \mathrm{d}\vec{\varepsilon}_v = (\mathrm{d}\varepsilon_v, \mathrm{d}\varepsilon_v, \mathrm{d}\varepsilon_v, 0, 0, 0) \tag{3}$$

with $K = \lambda + \frac{2}{3}\mu$, the compressibility (elastic) modulus. We define s_i and e_i two vectors of dimension six corresponding to the deviatoric part of the stress and strain tensors, respectively:

$$e_i = \begin{cases} \varepsilon_i - \varepsilon_v/3 & \text{if } i \in \{1, 2, 3\}, \\ \varepsilon_i & \text{otherwise,} \end{cases}$$
$$s_i = \begin{cases} \sigma_i - \sigma_M & \text{if } i \in \{1, 2, 3\}, \\ \sigma_i & \text{otherwise.} \end{cases} \tag{4}$$

Then, a family of imbricated yield surfaces (the Von Mises criterion) is defined by $F_n(\vec{s}, \vec{\alpha}^n) = k_n^2$, with $k_n \in \mathbb{R}$ a constant associated with the nth surface that will be defined later. $\vec{\alpha}^n$ refers to the centre of the nth surface. F_n and its derivative write:

$$F_n(\vec{s}, \vec{\alpha}^n) = \frac{1}{2}\Big(\left(s_1 - \alpha_1^n\right)^2 + \left(s_2 - \alpha_2^n\right)^2 + \left(s_3 - \alpha_2^n\right)^2 + 2\left(s_4 - \alpha_4^n\right)^2 + 2\left(s_5 - \alpha_5^n\right)^2 + 2\left(s_6 - \alpha_6^n\right)^2\Big) \tag{5}$$

and

$$\frac{\partial F_n(\vec{s}, \vec{\alpha}^n)}{\partial s_i} = \begin{cases} \left(s_i - \alpha_i^n\right) & \text{if } i \in \{1, 2, 3\}, \\ 2\left(s_i - \alpha_i^n\right) & \text{otherwise.} \end{cases} \tag{6}$$

Then, we write the deviatoric part of the strain tensor as the contribution of elastic and plastic parts,

$$\mathrm{d}\vec{e} = \left(\frac{1}{2G_0}\underline{\vec{I}}_6 + \underline{\vec{A}}\right)\mathrm{d}\vec{s}, \tag{7}$$

where G_0 is the shear-modulus (i.e. the μ Lamé coefficient), $\underline{\vec{I}}_6$ is the 6×6 identity matrix and the $\left(\underline{\vec{A}}\right)_{ij}$ are given by,

$$\left(\underline{\vec{A}}\right)_{ij} = \sum_{n=1}^{N} \frac{L_n \left(\partial F_n \left(\vec{s}\right)/\partial s_i\right)\left(\partial F_n \left(\vec{s}\right)/\partial s_j\right)}{C_n \sum_{k=1}^{6} \left(\partial F_n \left(\vec{s}\right)/\partial s_k\right)^2}, \tag{8}$$

where L_n is the 'activity index' of the nth surface, equal to 0 if the surface is inactive and equal to 1 if active. C_n is a constant associated with the nth surface.

The nth surface is active ($L_n = 1$) if,

$$F_n \left(\vec{s}, \vec{\alpha}^n\right) = k_n^2 \quad \text{and} \quad \sum_{k=1}^{6} \frac{\partial F_n \left(\vec{s}, \vec{\alpha}^n\right)}{\partial s_k} \mathrm{d}s_k \geq 0, \tag{9}$$

and $L_n = 0$, otherwise. Note that, because $\{k_n\}_{n=1,\ldots,N}$ is an increasing succession, if the nth surface is inactive ($L_n = 0$), it is also the case for the successive surfaces, $L_i = 0$ for $i = n+1, n+2, \ldots, N$. As the actual value of $\mathrm{d}s_k$ is unknown, the evaluation of (9) is done with the $\mathrm{d}s_k$ estimate at the previous time step with no impact on the solution (Joyner & Chen 1975).

At each time step, the linear system (7) is solved to obtain $\vec{\mathrm{d}s}$ given $\vec{\mathrm{d}e}$. If the nth surface has been activated (i.e. $L_n = 1$), then its centre should be adjusted by

$$\alpha_i^n := s_i - \frac{k_n}{\sqrt{F_n \left(\vec{s}\right)}} \left(s_i - \alpha_i^n\right). \tag{10}$$

This equation allows to update each active surface centre to slide and follow the actual stress state (as described in Fig. 1). Once the deviatoric stress increments are determined and the surface centres are updated, the total stress increments are calculated as

$$\mathrm{d}\sigma_i = \mathrm{d}s_i + \begin{cases} \mathrm{d}s_M & \text{if } i \in \{1,2,3\}, \\ 0 & \text{otherwise,} \end{cases} \tag{11}$$

where $\mathrm{d}s_M$ is the increment in mean stress. Finally, the stress is updated by

$$\vec{\sigma} := \vec{\sigma} + \vec{\mathrm{d}\sigma}. \tag{12}$$

The last point concerns the determination of constants k_n and C_n, associated with the nth yield surface. Considering the case of simple shear along one principal direction, without loss of generality, s_4 and e_4 can be set as the only components different from zero. The parameter k_n represents the yield limit (in simple shear) for the nth surface. The set of k_n values is chosen to cover the whole range of shear stress. The set of e_k, $(k = 1, N)$ is associated with these values. In the later case of simple shear, the relation (7) reduces to

$$\mathrm{d}e_4 = \frac{\mathrm{d}s_4}{2G_0} + \left(\underline{\vec{A}}\right)_{44} \mathrm{d}s_4 \tag{13}$$

$$= \left(\frac{1}{2G_0} + \sum_{n=1}^{j} \frac{1}{C_n}\right) \mathrm{d}s_4, \tag{14}$$

where j is the index of the last active surface. Writing $\mathrm{d}e_4 = e_{j+1} - e_j$ and $\mathrm{d}s_4 = k_{j+1} - k_j$, the following recurrence relation is obtained :

$$\frac{1}{C_j} = \frac{e_{j+1} - e_j}{k_{j+1} - k_j} - \frac{1}{2G_0} - \sum_{n=1}^{j-1} \frac{1}{C_n}, \tag{15}$$

where the first term represents what is accommodated by the jth Iwan element, the second one is the linear part and the last term represents what has been accommodated by the previous elements. The values of k_{N+1} and e_{N+1} (not defined) are set equal to the maximum shear stress and strain, respectively.

3 DISCRETIZATION OF THE MODULUS REDUCTION CURVE

When an explicit formula relating stresses and strains is available, the algorithmic complexity of a nonlinear constitutive relation between stress and strain may be independent on the level of strain reached. Therefore, the cost of one stress–strain evaluation per node is constant. On the contrary, the Iwan model is based on a set of imbricated yield surfaces. At each stress–strain evaluation, we need to establish how many of these surfaces are active. Then the complexity, and consequently the computational cost, is proportional to $AS(\boldsymbol{\varepsilon})$, which represents the number of active surfaces that are needed to reach a strain level $\boldsymbol{\varepsilon}$. It is thus advisable to arrange these hypersurfaces suitably so as to cover the *a priori* expected strain range reached in the simulation. In the recent literature, the choice of $N = 50$ surfaces logarithmically distributed between the minimum and maximum strain levels is commonly used (Bardet & Tobita 2001; Santisi d'Avila *et al.* 2012; Pham 2013; Mercerat *et al.* 2015; Oral *et al.* 2017). Even if one of the first proposals applying the elastoplastic Iwan model in site response analysis by Joyner (1975) promoted the use of linearly sampled yield stresses, subsequent implementations of the model almost exclusively used logarithmically distributed strain sampling of the shear modulus reduction curve. In soil dynamics, it is also common to use hyperbolic models, as introduced by Hardin & Drnevich (1972), because they satisfactorily fit laboratory observations. In 1-D, the nonlinear relationship between stress and strain reduces to $\sigma(\varepsilon, x) = \mu_{\max}(x) G(\varepsilon, x)\varepsilon(x)$ where $\mu_{\max}$ is the shear-modulus and $G(\varepsilon, x) = \mu(\varepsilon, x)/\mu_{\max}$ is the shear-modulus ratio which represents the nonlinearity

$$G(\varepsilon, x) = \frac{1}{1 + \frac{|\varepsilon|}{\gamma_{\mathrm{ref}}}}, \tag{16}$$

which only depends on γ_{ref}, the reference shear strain of the soil, that is the strain value corresponding to $G(\varepsilon = \gamma_{\mathrm{ref}}) = 0.5$. Here, we select $\gamma_{\mathrm{ref}} = 10^{-3}$. A typical modulus reduction curve is presented in Fig. 2. Only for illustration, N is set to 30. From Fig. 2 (left), it can be deduced that in the low strain range ($\gamma < 10^{-6}$) where a rather flat $G(\varepsilon, x)$ is found, around seven hypersurfaces have been activated. In the intermediate strain range, more elements are needed to better represent high variations in the modulus reduction curve. This observation motivates the use of the sampling technique described in the next section.

3.1 Equipartition algorithm

We present here the technique we applied for the automatic sampling of the shear-modulus reduction curve. The method is directly transposed from Nishikawa (1998). Following the shear-modulus reduction curve, the automatic procedure places as many points as necessary to approximate the curve by piecewise linear interpolation with an error lower than a given tolerance (in L_2-norm for example). It must be noted that values of the function and its derivative must be known at each sampling point. In our case, a hyperbolic least-squares fitting is done, and the analytical derivative is used. The method can be used in two ways. First, we can fix the acceptable error level all along the expected strain range and then find the appropriate number N of surfaces to be used, or we can set the number of surfaces N and, by successive linear approximations, place the sampling points at locations that minimize the error. We choose to exploit the second way in order to improve the reduction curve approximation and avoid to define an acceptable error level. From the implementation point of view, it seems easier to keep the

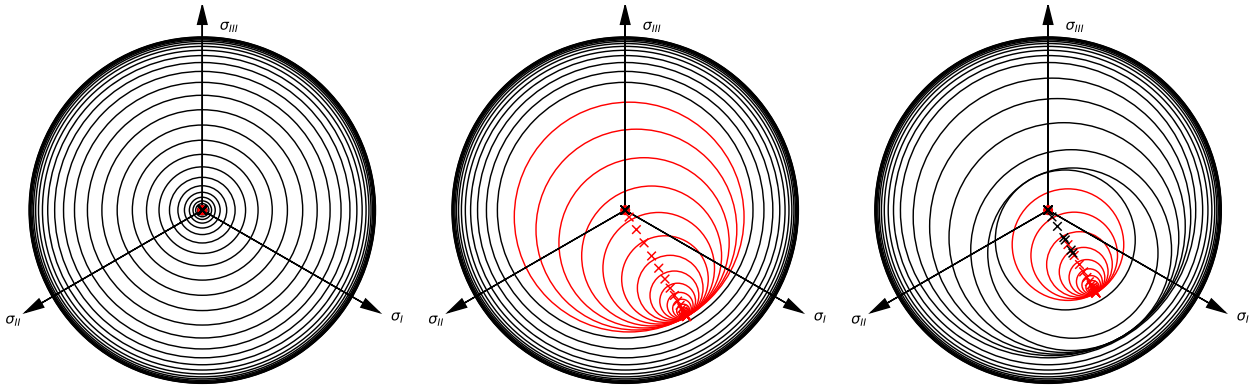

Figure 1. Yield surfaces evolution (the Von Mises criterion) in the principal stresses plane. An isometric projection was used from 3-D to 2-D plot. The normal to the plane is the deviatoric stress axis ($\sigma_{\rm I} + \sigma_{\rm II} + \sigma_{\rm III} = 0$). The active surfaces are shown in red, their centres are marked by crosses. The colour version of this figure is available only in the electronic edition.

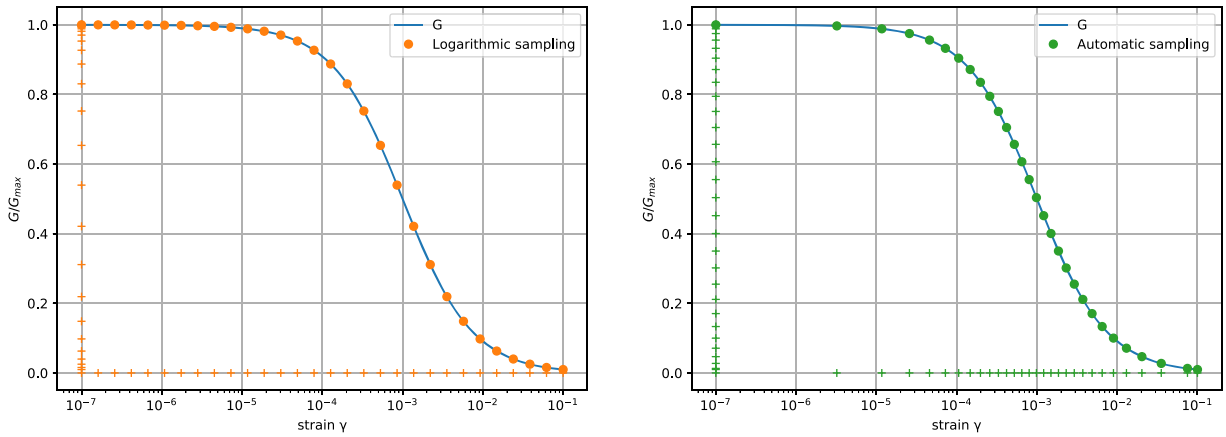

Figure 2. Sampling of a standard shear-modulus reduction curve. For a better visualization, N is set to 30. Classical method, that is logarithmically equispaced (left) and automatically spaced (right). Crosses added to both axes correspond to the stress/strain sampling values, represented by dots on the curves. The colour version of this figure is available only in the electronic edition.

same number of Iwan elements for all nonlinear media. Moreover, our objective is to reduce the total computation time of the simulation without accuracy loss. More details about the technique and the error analysis can be found in Nishikawa (1998).

Given a function $G(\gamma)$ together with its first derivative $F(\gamma)$ in the interval $I = [\gamma_{\min}, \gamma_{\max}]$, the method aims to construct a piecewise linear continuous approximation $g(\gamma)$ satisfying a given error criterion. The interval I is discretized into a set of elements $\{E\}$ with $E = [\gamma_l, \gamma_r]$ and $\Delta\gamma_E = \gamma_r - \gamma_l$ is supposed to be small. The L^2 error in E is defined by

$$\|G - g\|^2_{L^2(E)} = \int_E [G(\gamma) - g(\gamma)]^2 \, {\rm d}\gamma. \tag{17}$$

Supposing that g is constructed in E with exact nodal values at boundaries, that is $g_l = g(\gamma_l) = G(\gamma_l)$ and $g_r = g(\gamma_r) = G(\gamma_r)$, the restriction of g to E writes

$$g_{|E}(\gamma) = \frac{\Delta g_E}{\Delta\gamma_E}\gamma + \frac{g_l\gamma_r - g_r\gamma_l}{\Delta\gamma_E}, \tag{18}$$

where $\Delta g_E = g_r - g_l$.

From Nishikawa (1998), the error reduces to

$$\|G - g\|^2_{L^2(E)} = \frac{\Delta F_E^2 \Delta\gamma_E^3}{120} + O\left(\Delta\gamma_E^6\right), \tag{19}$$

where $\Delta F_E = F(\gamma_r) - F(\gamma_l)$ or also

$$\|G - g\|_{L^2(E)} = \mathcal{E}_E\left[1 + O(\Delta\gamma_E^2)\right], \tag{20}$$

with the notations

$$\mathcal{E}_E = \frac{C_E\sqrt{\Delta\gamma_E}}{\sqrt{120}} \text{ and } C_E = \Delta F_E \, \Delta\gamma_E \, . \tag{21}$$

From the initial point $(\gamma_{\min}, G(\gamma_{\min}))$, the algorithm generates the node distribution or equivalently the elements E of $\{E\}$ so as to equally distribute C_E over the elements. The consequence is a concentration of nodes in the region of large $|{\rm d}^2G/{\rm d}\gamma^2|$. Supposing that the error criterion is constant over the entire domain, $C_E = C$, the global error in I is written in a similar way to eq. (20) for E with

$$\mathcal{E}_I^2 = \sum_{\{E\}} \frac{C_E^2\Delta\gamma_E}{120} = \frac{C^2}{120}(\gamma_{\max} - \gamma_{\min}) \, . \tag{22}$$

Once the set of elements E is constructed (depending on C) the approximation g is recovered using the values $G(\gamma_j)$ at the sampling points γ_j; the error estimate is second-order accurate.

To generate γ_{j+1} from γ_j and define $E = [\gamma_j, \gamma_{j+1}]$, we need to iterate γ_{j+1} until we have

$$(\gamma_{j+1} - \gamma_j)\,|\Delta F_E| - C = 0, \tag{23}$$

with $\Delta F_E = F(\gamma_{j+1}) - F(\gamma_j)$. The iteration formula which is applied is

$$rl\gamma_{j+1}^{(k+1)} = \gamma_j + \left[\frac{C\left(\gamma_{j+1}^{(k)} - \gamma_j\right)^{p-1}}{|\Delta F_E^{(k)}|}\right]^{1/p} = \gamma_j + \left(\gamma_{j+1}^{(k)} - \gamma_j\right)\left[\frac{C}{C_E^{(k)}}\right]^{1/p}, \quad (24)$$

where k is the number of iterations (≥ 1), p is a positive real number and $C_E^{(k)} = (\gamma_{j+1}^{(k)} - \gamma_j)\Delta F_E^{(k)}$. At convergence (23) is satisfied.

The algorithm to compute the position of the nodes in the strain axis between $[\gamma_{\min}, \gamma_{\max}]$ reads,

(1) Given global error (or N nodes), compute $C = \mathcal{E}_I\sqrt{120}$.
(2) From γ_j, set $\gamma_{j+1}^{(k)} = \gamma_j + (\gamma_j - \gamma_{j-1})$, $C_E^{(k)} = (\gamma_{j+1}^{(k)} - \gamma_j)\Delta F_E^{(k)}$.
(3) Compute the new location $\gamma_{j+1}^{(k+1)} = \gamma_j + (\gamma_j^{(k)} - \gamma_j)\left[\frac{C}{C_E^{(k)}}\right]^{1/p}$.
(4) If $|C/C_E^{(k)} - 1| < \mathrm{TOL}$, goto (3).
(5) If $\gamma_{j+1} \leq \gamma_{\max}$, goto (2) (next node).
(6) Evaluate $G(\gamma_i)$ at $i = 1,..., N$.

For any value of shear strain lower than 10^{-2}, the automatic sampling distributes fewer active surfaces than the logarithmic sampling (Fig. 2). The difference between sampling methods is even greater when the strain is below 10^{-3}. For large deformations ($>10^{-2}$ in this example), the two approaches are equivalent (i.e. should exhibit comparable computation times) although the shear-modulus reduction curve is better approximated using the automatic sampling than the logarithmic one.

4 NUMERICAL EXAMPLES

Two numerical applications aim to quantify the reduction of computational cost associated with the implementation of the Iwan model by means of the automatic sampling technique. Both are based on the solution of the elastodynamic system of equations written in the velocity–strain formulation and discretized by a nodal discontinuous Galerkin finite element method (Chabot 2018). The problem unknowns are approximated using fourth-order Lagrange polynomial interpolation and centred fluxes are applied at interfaces between elements. The explicit time scheme is a low-storage fourth-order Runge–Kutta method (Carpenter & Kennedy 1994; Hesthaven & Warburton 2008). This method is preferred over a classical Runge–Kutta method because the successive steps of the iterative method involve increasing times, which is better suited to take into account hysteresis. The mesh is constructed so as to place ten interpolation points per minimal wavelength, which corresponds to approximately 2.5 mesh elements per minimal wavelength. The proposed sampling technique is independent of the numerical method used to solve these equations, we do not detail it here, but some key elements are provided when necessary in the following sections.

4.1 1D-3C case

For this first test, we consider the case of a coupled unidimensional propagation in a complex soil column inspired from the Euroseis-Test Site (Raptakis *et al.* 2019). This test case has already been proposed in our original paper Chabot *et al.* (2018) considering the logarithmically equispaced method. We propose here to compare the results when the two sampling methods (*logarithmic* and *automatic*) are applied to the shear-modulus reduction curve. We study the wave propagation in a 1-D heterogeneous soil model containing five layers, all nonlinear, each characterized by a hyperbolic model described by eq. (16). The numerical model is 196 m deep and the properties of the media composing the soil column are from Guéguen (2016) and listed in Table 1. The mesh of the 1-D domain is non-uniform, the criterion being adapted to the shear wave velocity in each layer. The 1D-3C solver is written in Cython, an extension of Python compiled in C, which yields a performance gain in the 1D-3C case.

The wave propagates from the bottom of the soil column up to the free surface. The three components of motion are considered, hence the name 1D-3C (i.e. unidimensional propagation, three components of motion). Unlike the linear case, the nonlinear material behaviour results in coupling effects between the different components of motion which justifies the study of the three components simultaneously. A free surface condition at the top is set while a rigid boundary condition at the base of the model ($z = -196$ m) is applied by imposing the three components of the velocity field. The input motion is a Gabor wavelet of central frequency $f_0 = 3$ Hz and maximum amplitude $A = 10^{-2}$ m s^{-1} imposed at 196 m depth which is the bottom limit of our numerical model. Both horizontal components of motion are excited, with a phase difference of $\pi/2$, to simulate a circular wave polarization and to explicitly couple both horizontal components.

Regardless of the type of sampling, $N = 50$ elements are used for all nonlinear media. All parameters of the simulations remain the same, only the sampling method of the shear-modulus reduction curve differs. To measure the impact of sampling, we compare the two methods to a reference solution. This reference solution is calculated up to $T = 20$ s with logarithmic sampling and an extremely high number of elements ($N = 300$). For each simulation, we measure both the calculation times relative to the linear case (i.e. the ratio between computation times corresponding to nonlinear and linear simulations), the number of active surfaces of the Iwan model, and the error with respect to the reference solution, calculated at the receiver located at the free surface. The results are given in Table 2.

We can deduce from Table 2 that, when 50 elements are used, the relative error is almost identical at the end of the simulation whatever the sampling method, but the computation time has been significantly reduced by 75 per cent with respect to the simulation based on logarithmic sampling. Using automatic sampling and a higher number of Iwan elements per node (150), the error with respect to the reference solution is only 0.25 per cent whereas the saving of time is about 56 per cent. For a simulation time twice as long, the relative error has been divided by ten.

The evolution throughout the simulation of the computation time necessary to advance the simulation of a fixed amount of physical time (here 0.05 seconds) is compared in Fig. 3 (left panel). When the Iwan elastoplastic model is used, a call to the stress-strain function depends on the absolute value of the shear strain (i.e. related to the number of active surfaces in the Iwan model). The first iterations are longer to calculate, since larger deformations imply more active surfaces. We also notice that the variations in calculation time are more important in the case of logarithmic than in the case of automatic sampling because of a larger number of Iwan elements in the portion of the curve corresponding to lower strains. In other words, the calculation time of the proposed method is less sensitive to variations in the shear deformation level. This is all the more visible for $N = 150$ for which the automatic sampling is more efficient than the

Table 1. Characteristics of the materials composing the soil column. The upper coordinate of medium layer L is denoted by z (in m), ρ^L is the density (kg m^{-3}), v_s^L and v_p^L (m s^{-1}) are the shear and compressional waves velocities respectively. Finally, γ_{ref}^L and Q^L are the reference shear strain and the quality factor, both dimensionless.

Layer number	z	ρ^L	v_s^L	v_p^L	Soil type	γ_{ref}^L	Q^L
1	0	2111	200	795	Silty clay sand	5.04×10^{-4}	20
2	−18	2104	345	1371	Silty sand and sandy clay	3.96×10^{-4}	25
3	−40	2089	358	1530	Silty-silty sand, sandy clay	3.23×10^{-4}	30
4	−73	2157	496	2015	Sandy clay or silty clay with gravels	1.49×10^{-3}	40
5	−136	2250	714	2446	Silty clay sand	5.04×10^{-4}	80

Table 2. Relative computation times with respect to a linear simulation (ratio between nonlinear and linear simulation), cumulative number of active surfaces for the whole simulation, and relative error in L2-norm against the elastoplastic reference solution ($N = 300$) for different sampling methods and number of elements.

Sampling method	N	Time ratio	Cumulative active surfaces	Relative error (per cent)
Logarithmic	50	343	107 060	2.33
Automatic	50	87	28 624	2.31
Automatic	150	150	76 735	0.25

Notes: The calculations have been performed on a laptop computer with an Intel Core i7 3.1 GHz. For information, the computing time for the linear solution is around 44 s, and the one of the reference elastoplastic solution around 14 hr.

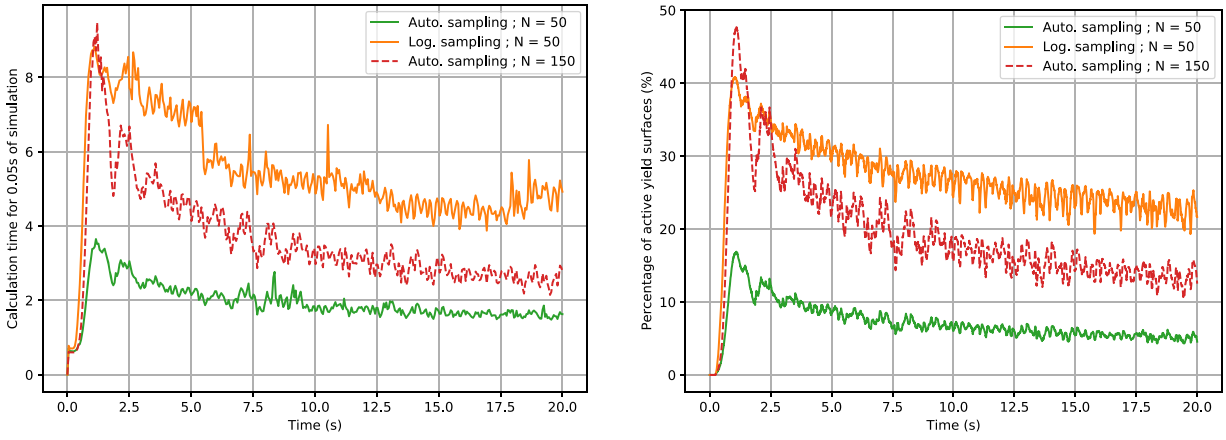

Figure 3. Left: evolution throughout the simulation of the computational time required to perform 0.05 s of simulation for elastoplastic cases with logarithmic with $N = 50$ (orange), automatic with $N = 50$ (green) and $N = 150$ (dashed red) samplings of the shear-modulus reduction curve. Right: evolution of the percentage of active surface during the simulation for the same cases. Comparison between logarithmic (orange) and automatic (green) sampling strategies with $N = 50$. The colour version of this figure is available only in the electronic edition.

logarithmic one with $N = 50$. We are also interested in the evolution during the simulation of the percentage of active surfaces necessary in the Iwan model (Fig. 3, right panel). Up to 40 per cent of the surfaces are used at the beginning of the process with the logarithmic sampling while this number does not reach 20 per cent for the automatic sampling. This difference also remains at low strains at the end of the simulation, the proposed method making it possible to reduce the necessary surfaces from 22 per cent to only 5 per cent, which explains the differences in the total computation time.

To compare the accuracy of different sampling algorithms, we plot the velocity seismograms at the surface of the model ($Z = 0$ m) and the stress–strain curves at a specific depth ($Z = -15$ m) in the nonlinear soil column (Fig. 4). First, all the three traces match almost perfectly the reference. We observe in the first inset window, a zoom on a local maximum, for an identical number of elements ($N = 50$ in this case). The solution obtained with the automatic sampling is significantly closer to the reference than that obtained with the logarithmic sampling. On the other hand, if we observe the second time window around $t = 11.7s$, we notice that a phase-shift gradually appears. This shift is less visible with logarithmic sampling probably because the logarithmic sampling better approximates the shear-modulus reduction curve at lower strains, which *in fine* could reduce the phase shift. Nevertheless, the gain in terms of calculation time outperforms this slight phase difference. Finally, we note that the solution obtained with automatic sampling and $N = 150$ Iwan elements—twice as fast as the one with logarithmic sampling and 50 elements—is almost similar to the reference solution, while being seven times faster to calculate.

4.2 3D-3C case

We now compare the two sampling methods in a 3-D case. We propose, in particular, to evaluate the computation time of an

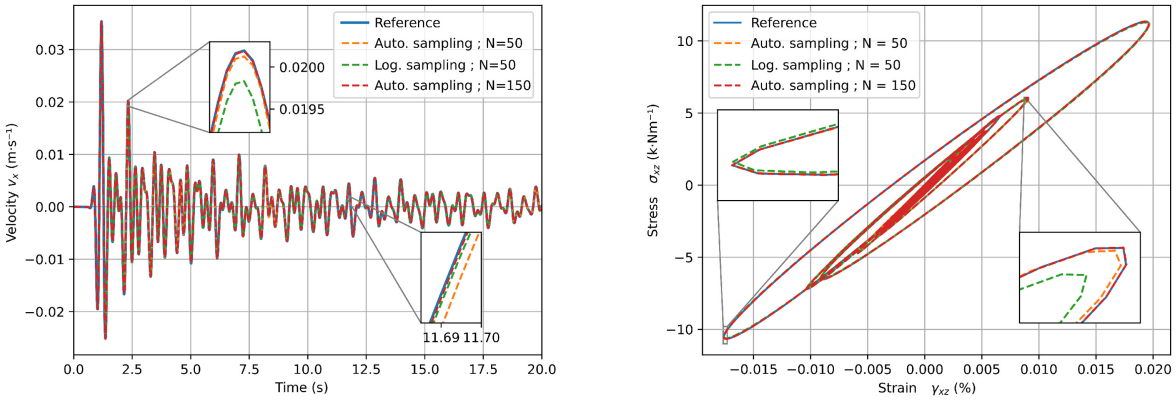

Figure 4. Left: horizontal velocity seismograms simulated at the surface of the soil column ($Z = 0$ m) for the three different modulus reduction sampling cases of Table 2. Right: corresponding stress–strain loops in the surface layer at $Z = -15$ m. The colour version of this figure is available only in the electronic edition.

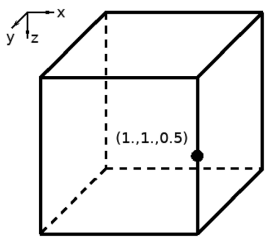

Figure 5. Unit cube cavity used for the 3-D application and location of the visualization point.

elastoplastic simulation with respect to the input motion amplitude level. The idea is to check the hypothesis that the cost of the simulation is proportional to the number of active surfaces and therefore directly related to the maximum strain reached during the simulation. We consider the vibration of an eigenmode in the three dimensions of space following what was proposed for a linear medium in Delcourte & Glinsky (2015). The computation domain is the unit cube cavity, as described in Fig. 5, on which free surface conditions are applied for the six cube faces. An exact solution in space and time in velocity–stress formulation, considering a linear medium, is presented in Appendix A. The medium is supposed to be homogeneous with dimensionless physical properties equal to $\rho = 1$ kg m^{-3}, $v_p = 1$ m s^{-1} and $v_s = 0.5$ m s^{-1}, density, compressional and shear wave velocities, respectively. An initial condition at $t = 0$ is deduced for the velocity-strain system from the exact solution of Appendix A. The system will freely vibrate until $t = 100$ s. For the application of the MPII model in the elastoplastic case, an hyperbolic model with $\gamma_{\text{ref}} = 5$ is considered. This value is not realistic but adapted to the dimensionless medium properties. This initial condition remains valid only at $t = 0$ in the elastoplastic case. A uniform mesh is constructed by dividing the domain in 10^3 cubic cells that are split into six tetrahedra. Assuming that the nonlinearity causes a decrease up to 50 per cent in v_s, the mesh size would allow an accurate solution up to 2.5 Hz.

The comparison between linear and elastoplastic solutions is shown in Fig. 6 that presents the time evolution of the X-velocity component in point (1.0,1.0,0.5) until time $t = 100$ s. A decrease in the propagation velocity and in the amplitude of the X-velocity component is observed in the nonlinear case. The propagation velocity decreases due to the shear-modulus reduction which results in a phase shift of the modal frequency peak compared to the linear case. The reduction in amplitude is due to the hysteretic damping which depends on the area of the hysteresis loops and therefore on the velocity amplitude. From a certain time (around $t = 70$ s), nonlinear effects are no longer distinguished, that is the material returns to behave elastically and there are no more damping and wave velocity changes in the medium. The Fourier spectra of the X-velocity component shows the shift of the main fundamental frequency of the excited mode, but also the excitation of higher modes (around 1 Hz) due to nonlinearity. From the comparison of the velocity at the cube surface for four multiples of the period T_0 (Fig. 7), we first observe that the velocity field remains the same when the medium is linear (figures on the left). The damping and the phase shift are clearly visible in the elastoplastic case (figures on the right), resulting in a reduction in the surface velocity amplitude, accordingly to the results of Fig. 6.

To study the influence of the input motion amplitude, the medium properties are kept unchanged but the initial condition amplitude is multiplied by a factor α. Note that in the linear case, $(\alpha \bar{V}, \alpha \boldsymbol{\sigma})$ of eq. (A1) remains an exact solution of the problem. The X-velocity component time solution is the same as the case $\alpha = 1$ (Fig. 6) but with vertical scale multiplied by α. Moreover, the computation time only depends on the final physical time of the simulation and not on the value α or the maximum strain. We vary α between 10^{-5} and 10, the value $\alpha = 1$ corresponding to the initial case. In the elastoplastic case, according to the value of α, more or less surfaces will be activated impacting the calculation time. The shear-modulus reduction curve remains the same with $\gamma_{\text{ref}} = 5$ and the two sampling methods (logarithmic and automatic) are applied. As in the previous test, the number of Iwan elements is set to $N = 50$ and the simulation corresponds to the physical time $t = 100$ s. For different values of α, we calculate the ratio between CPU times of elastoplastic and linear calculations.

As expected, we observe that the relative computational time depends on the input motion amplitude (Fig. 8). When the logarithmic sampling is applied, the MPII model surfaces are equispaced in logarithmic scale. Varying α equidistantly in a logarithmic scale, it is therefore logical to find a CPU cost proportional to α. However, in the case of automatic sampling, these surfaces are not equispaced in logarithmic scale but located at best. So, for a given strain level (or equivalently a value of α), fewer surfaces are activated and the computation time is reduced. For values of α between 10^{-4} and

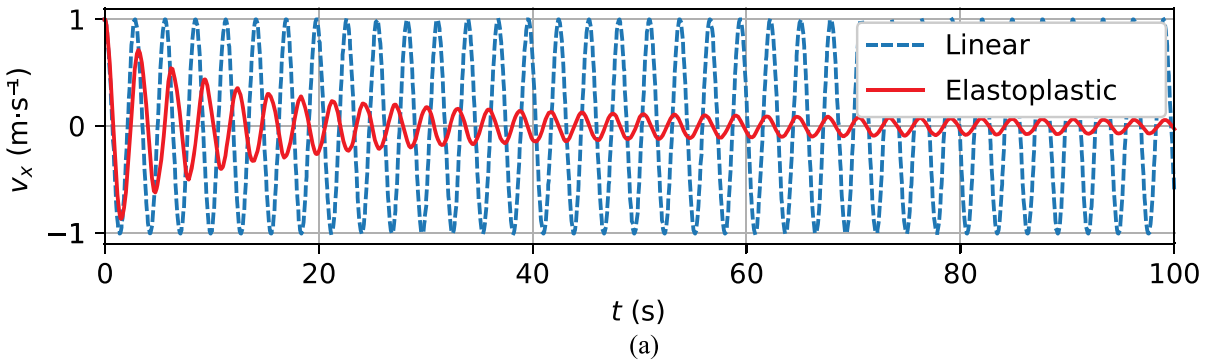

(a)

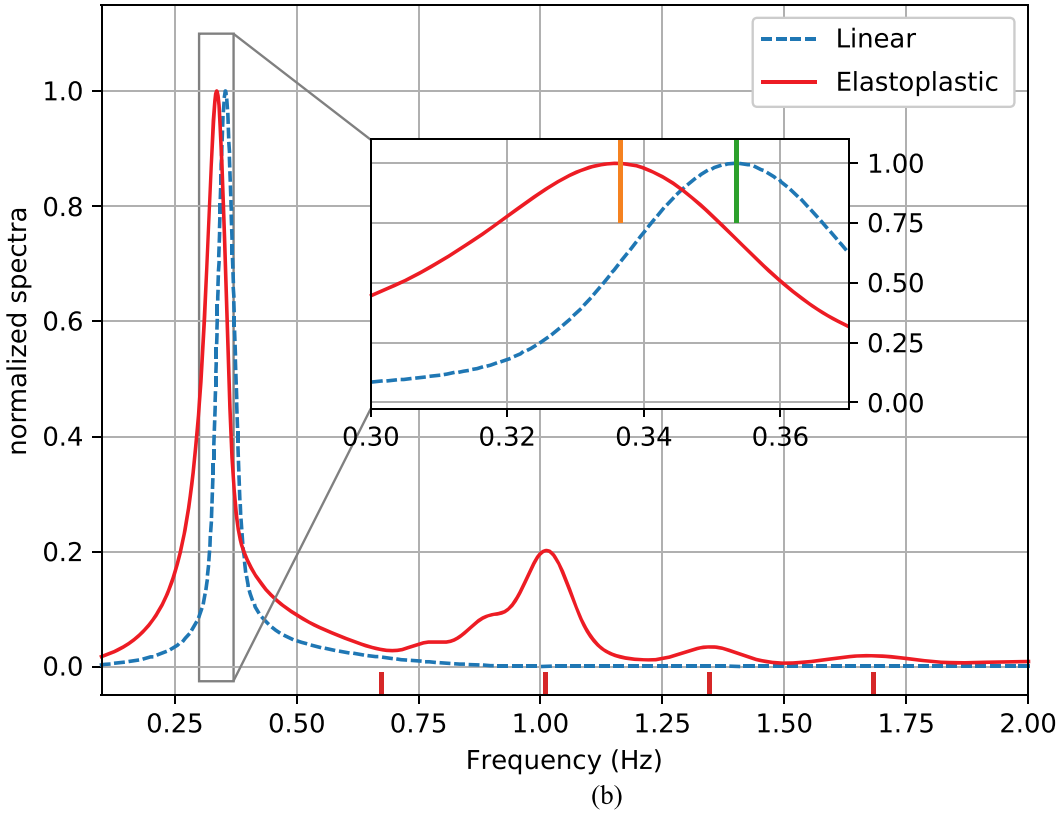

(b)

Figure 6. (a) Time evolution of the X-component of velocity at point (1.0,1.0,0.5) for linear and elastoplastic media ($\gamma_{\text{ref}} = 5$). (b) Normalized Fourier spectra of the previous traces. The colour version of this figure is available only in the electronic edition.

2.0×10^{-1}, the extra cost of the nonlinear simulation with respect to the linear case remains stable between 15 and 20 when the automatic sampling is applied. This is not the case when the logarithmic sampling is used, the extra cost increases to 70 for this range of α values.

5 CONCLUSIONS

We studied the impact of different sampling algorithms to approximate the shear-modulus reduction curve in the context of nonlinear wave propagation using the elastoplasic Iwan model. This curve is the only input required for the nonlinear model. Compared to the classical logarithmic sampling of the shear-modulus reduction curve, the proposed automatic sampling algorithm significantly reduces the computation time. It is possible to reduce the error of the approximation for the shear-modulus reduction curve, while keeping a constant number of Iwan elements per node. Therefore, the memory requirements of the numerical simulation are not increased unlike the case of logarithmic sampling. We proved that the computation cost of the nonlinear model depends on the strain level reached in the simulation. By using the automatic sampling technique, it is possible to reduce the number of active surfaces and consequently the computation time with an even greater impact for a numerical simulation in a 3-D medium. From the computational point of view, the approximation of the shear-modulus reduction curves are performed once, before the wave-propagation simulation and simply requires the storage of the vector with the strain sampling points for each reduction curve to be used. Finally, this sampling technique is applicable whatever the numerical method used for the wave propagation and results in a significant gain in computation time, particularly interesting for 3-D simulations.

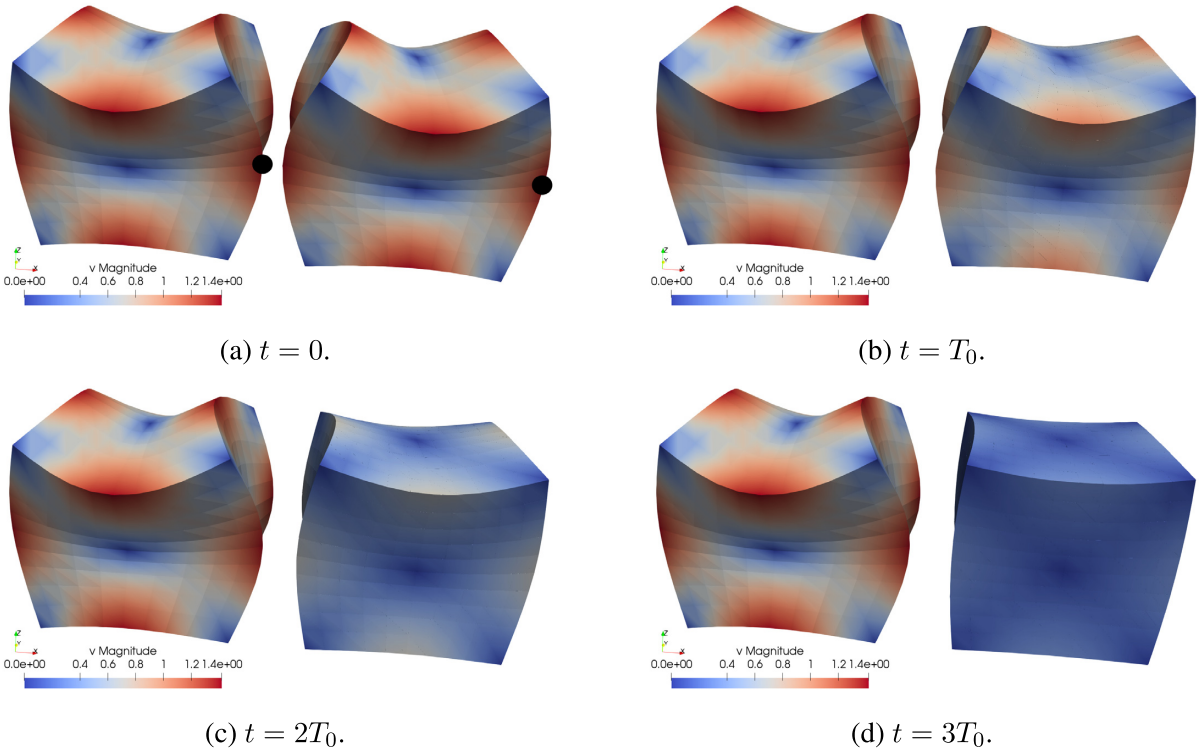

(a) $t = 0$. (b) $t = T_0$.

(c) $t = 2T_0$. (d) $t = 3T_0$.

Figure 7. Time evolution of the velocity field for the propagation of an eigenmode problem in the 3-D cube. The receiver location is marked by black circles. At each snapshot, the linear elastic cube (left panels in each snapshot) is compared to the nonlinear elastoplastic cube (right panels). The velocity fields are plotted at four different times, $T_0 = 2\sqrt{2}$ being the period of the excited mode in the linear case, what gives exactly the same field. For visualization purposes, each node is displaced proportionally to the corresponding velocity vector. The colour version of this figure is available only in the electronic edition.

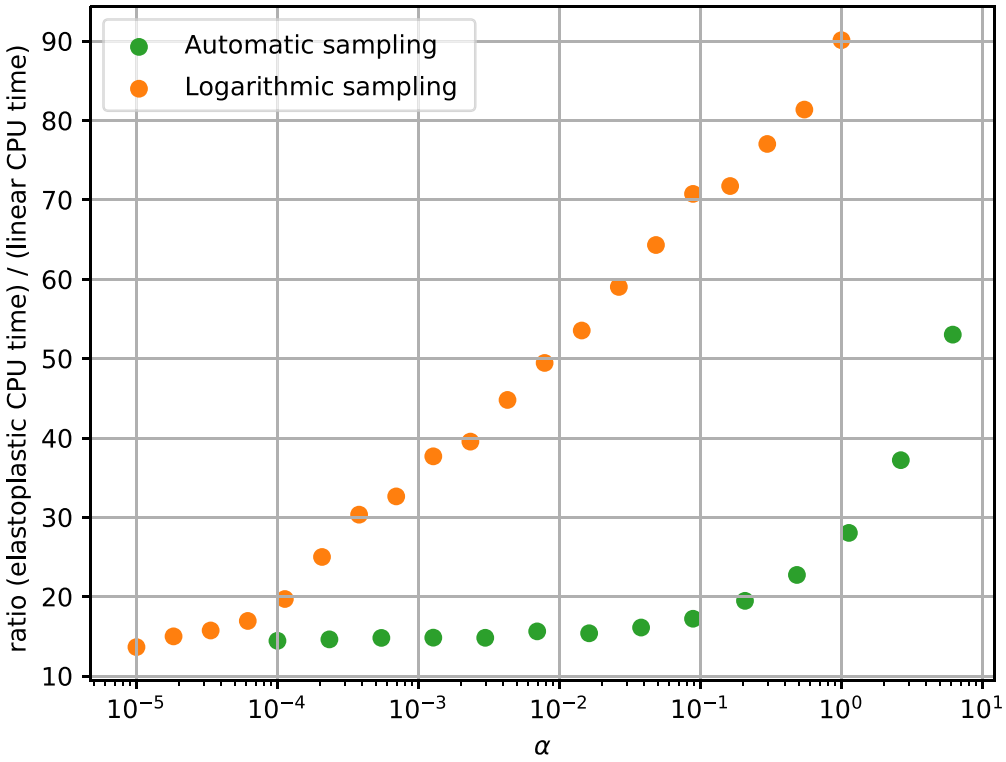

Figure 8. Relative computational time for the 3-D simulations as a function of the initial amplitude factor α for logarithmic and automatic sampling of the shear-modulus reduction curve. Calculations were done using a quadri Intel Core I5 3.3 GHz personal computer. The colour version of this figure is available only in the electronic edition.

ACKNOWLEDGEMENTS

The authors acknowledge the insightful comments and remarks of two anonymous reviewers that helped to write the final version of the manuscript. The Python routine to calculate the automatic sampling set of points (Equipartition algorithm) is available at https://github.com/chabotsi/ggmax-sampler.

DATA AVAILABILITY

The data underlying this paper are available in the paper and in its online supplementary material.

REFERENCES

Bardet, J.P. & Tobita, T., 2001. *NERA: A Computer Program for Nonlinear Earthquake Site Response Analyses of Layered Soil Deposits,* University of Southern California.

Carpenter, M.H. & Kennedy, C.A., 1994. Fourth Order 2N-Storage Runge-Kutta Schemes, Tech. Rep. 109112, NASA Langley Research Center.

Chabot, S., 2018. Modélisation numérique de la propagation des ondes par une méthode éléments finis Galerkin discontinue: prise en compte des rhéologies nonlinéaires des sols, *thèse de Doctorat*, Université Paris-Est.

Chabot, S., Glinsky, N., Mercerat, E.D. & Bonilla, L.F., 2018. A high-order discontinuous Galerkin method for coupled wave propagation in 1D elastoplastic heterogeneous media, *J. Theor. Comput. Acout.,* **26**(03), 1850043.

Chen, G., Jin, D., Zhu, J., Shi, J. & Li, X., 2015. Nonlinear analysis on seismic site response of Fuzhou Basin, China, *Bull. seism. Soc. Am.,* **105**(2A), 928–949.

Darendeli, M.B., 2001. Development of a new family of normalized modulus reduction and material damping curves, *PhD thesis*, University of Texas, Austin.

Delcourte, S. & Glinsky, N., 2015. Analysis of a high-order space and time discontinuous Galerkin method for elastodynamic equations. Application to 3D wave propagation, *Math. Modelling Numer. Anal.,* **49**(4), 1085–1126.

Gandomzadeh, A., 2011. Dynamic soil-structure interaction : effect of non-linear soil behavior, *thèse de Doctorat*, Paris Est.

Gélis, C. & Bonilla, L.F., 2012. 2-D *P–SV* numerical study of soil–source interaction in a non-linear basin, *Geophys. J. Int.,* **191**(3), 1374–1390.

Gélis, C. & Bonilla, L.F., 2014. Influence of a sedimentary basin infilling description on the 2-D *P–SV* wave propagation using linear and non-linear constitutive models, *Geophys. J. Int.,* **198**(3), 1684–1700.

Guéguen, P., 2016. Predicting nonlinear site response using spectral acceleration vs PGV/Vs30: a case history using the Volvi-test site, *Pure appl. Geophys.,* **173**(6), 2047–2063.

Hardin, B.O. & Drnevich, V.P., 1972. Shear modulus and damping in soils: measurement and parameter effects, *J. Soil Mech. Found. Div.,* **98**(6), 603–624.

Hesthaven, J.S. & Warburton, T., 2008. *Nodal Discontinuous Galerkin Methods,* Vol. 54, Springer New York.

Ishibashi, I. & Zhang, X., 1993. Unified dynamic shear moduli and damping ratios of sand and clay, *Soils Found.,* **33**(1), 182–191.

Iwan, W.D., 1966. A distributed-element model for hysteresis and its steady-state dynamic response, *J. Appl. Mech.,* **33**(4), 893–900.

Iwan, W.D., 1967. On a class of models for the yielding behavior of continuous and composite systems, *J. Appl. Mech.,* **34**(3), 612–617.

Joyner, W.B., 1975. A method for calculating nonlinear seismic response in two dimensions, *Bull. seism. Soc. Am.,* **65**(5), 1337–1357.

Joyner, W.B. & Chen, A.T.F., 1975. Calculation of nonlinear ground response in earthquakes, *Bull. seism. Soc. Am.,* **65**(5), 1315–1336.

Joyner, W.B., Warrick, R.E. & Fumal, T.E., 1981. The effect of quaternary alluvium on strong ground motion in the Coyote Lake, California, earthquake of 1979, *Bull. seism. Soc. Am.,* **71**(4), 1333–1349.

Lubliner, J., 1990. *Plasticity Theory,* Macmillan Publishing Company.

Mercerat, D. *et al.*, 2015. Modeling of 1D wave propagation in nonlinear soils using the elasto-plastic Iwan model by four numerical schemes, in *Proceedings of Seismological Society of America, 2015 Annual Meeting,* Pasadena, United States.

Mercerat, E.D. & Glinsky, N., 2015. A nodal discontinuous Galerkin method for non-linear soil dynamics, in *6th International Conference on Earthquake Geotechnical Engineering,* pp. 8, Christchurch, New Zealand.

Moczo, P., Kristek, J., Bard, P.-Y., Stripajova, S., Hollender, F., Chovanová, Z., Kristeková, M. & Sicilia, D., 2018. Key structural parameters affecting earthquake ground motion in 2D and 3D sedimentary structures, *Bull. Earthq. Eng.,* **16,** 2421–2450.

Nishikawa, H., 1998. Accurate Piecewise Linear Continuous Approximations to One-Dimensional Curves: Error Estimates and Algorithms, Tech. Rep.

Oral, E., Gélis, C., Bonilla, L.F. & Delavaud, E., 2017. Spectral element modelling of seismic wave propagation in visco-elastoplastic media including excess-pore pressure development, *Geophys. J. Int.,* **211**(3), 1494–1508.

Oral, E., Gélis, C. & Bonilla, L.F., 2019. 2-D *P–SV* and *SH* spectral element modelling of seismic wave propagation in non-linear media with pore-pressure effects, *Geophys. J. Int.,* **217**(2), 1353–1365.

Pham, V.A., 2013. Effets de la pression interstitielle sur la réponse sismique des sols: modélisation numérique 1D/3 composantes, *PhD thesis*, Université Paris-Est.

Poursartip, B., Fathi, A. & Tassoulas, J.L., 2020. Large-scale simulation of seismic wave motion: a review, *Soil Dyn. Earthq. Eng.,* **129,** 105909.

Prisco, C.D., Stupazzini, M. & Zambelli, C., 2007. Nonlinear SEM numerical analyses of dry dense sand specimens under rapid and dynamic loading, *Int. J. Numer. Anal. Methods Geomech.,* **31**(6), 757–788.

Raptakis, D., Theodulidis, N. & Pitilakis, K., 2019. Data analysis of the euroseistest strong motion array in Volvi (Greece): standard and horizontal-to-vertical spectral ratio techniques, *Earthq. Spectra,* **14,** 203–224.

Santisi d'Avila, M.P., Lenti, L. & Semblat, J.-F., 2012. Modelling strong seismic ground motion: three-dimensional loading path versus wavefield polarization, *Geophys. J. Int.,* **190**(3), 1607–1624.

Segalman, D.J. & Starr, M.J., 2008. Inversion of Masing models via continuous Iwan systems, *Int. J. Non-Linear Mech.,* **43**(1), 74–80.

Taborda, R., Bielak, J. & Restrepo, D., 2012. Earthquake ground-motion simulation including nonlinear soil effects under idealized conditions with application to two case studies, *Seismol. Res. Lett.,* **83**(6), 1047–1060.

Vucetic, Mladen & Dobry, Ricardo, 1991. Effect of soil plasticity on cyclic response, *J. Geotech. Eng.,* **117**(1), 89–107.

APPENDIX A: EIGENMODE SOLUTION IN 3-D

Considering an homogeneous linear elastic medium, an exact solution at time t and in $X = (x, y, z)$ of the (1,1,1) mode in the unit cube cavity is given for velocity and stress components by Delcourte & Glinsky (2015):

$$\begin{cases} v_x(t, X) = \cos(\pi x)\,[\sin(\pi y) - \sin(\pi z)]\,\cos(\Omega t) \\ v_y(t, X) = \cos(\pi y)\,[\sin(\pi z) - \sin(\pi x)]\,\cos(\Omega t) \\ v_z(t, X) = \cos(\pi z)\,[\sin(\pi x) - \sin(\pi y)]\,\cos(\Omega t) \\ \sigma_{xx}(t, X) = -A\,\sin(\pi x)\,[\sin(\pi y) - \sin(\pi z)]\,\sin(\Omega t) \\ \sigma_{yy}(t, X) = -A\,\sin(\pi y)\,[\sin(\pi z) - \sin(\pi x)]\,\sin(\Omega t) \\ \sigma_{zz}(t, X) = -A\,\sin(\pi z)\,[\sin(\pi x) - \sin(\pi y)]\,\sin(\Omega t) \\ \sigma_{xy}(t, X) = \sigma_{xz}(t, X) = \sigma_{yz}(t, X) = 0 \end{cases} \quad \text{(A1)}$$

with $A = \sqrt{2\,\rho\,\mu}$ and $\Omega = \pi\sqrt{2\mu/\rho}$. Dimensionless values are set for the medium properties, $\rho = 1$, $\lambda = 0.5$ and $\mu = 0.25$, which implies $v_p = 1$ and $v_s = 0.5$ through the relationships $v_p = \sqrt{\lambda + 2\mu/\rho}$ and $v_s = \sqrt{\mu/\rho}$. An equivalent condition for the system written in velocity-strain formulation is obtained by transforming the stress tensor $\boldsymbol{\sigma}$ into strain tensor $\boldsymbol{\varepsilon}$ through the relationship

$$\boldsymbol{\varepsilon} = \boldsymbol{C}^{-1}\boldsymbol{\sigma} \tag{A2}$$

where the compliance tensor writes

$$\boldsymbol{C}^{-1} = \frac{1}{E}\left[\begin{array}{ccc|ccc} 1 & -\nu & -\nu & & & \\ -\nu & 1 & -\nu & & 0_{3,3} & \\ -\nu & -\nu & 1 & & & \\ \hline & & & (1+\nu) & 0 & 0 \\ & 0_{3,3} & & 0 & (1+\nu) & 0 \\ & & & 0 & 0 & (1+\nu) \end{array}\right] \tag{A3}$$

with E and ν are the Young modulus and the Poisson ratio, respectively.